RSC Advances

PAPER

View Article Online
View Journal | View Issue

Cite this: *RSC Adv.*, 2026, **16**, 7355

Kinetic evolution of ZrO_2-modified silicate-based glass sealants during sintering and crystallization in planar solid oxide fuel cells

Shuai Yuan,[a] Haozhen Li,[a] Hao Shi,[a] Yuxuan Fei,[a] Hengyong Tu,[a] Chao Ma,*[b] Lei Zhu*[a] and Zhen Huang[ab]

Glass-composite sealants are critical for reliable high-temperature sealing in planar solid oxide fuel cells (SOFCs). This work investigates the influence of ZrO_2 on the sintering and crystallization kinetics of silicate-based glass-composite sealants. Dilatometry analysis reveals ZrO_2 promotes earlier densification and extends the sintering stage, with 200 nm particles exhibiting the strongest effect. Viscosity–temperature relationships, derived from differential scanning calorimetry (DSC) and the Vogel–Fulcher–Tammann model, indicate ZrO_2 increases viscosity by filling free volume, while excessive 50 nm ZrO_2 (>30 wt%) reduces viscosity due to nanoparticle agglomeration. Scanning electron microscopy (SEM) observations confirm that 200 nm ZrO_2 forms a rigid percolation framework, improving local sintering and promotes pore closure. X-ray diffraction analysis (XRD) indicates the incorporation of ZrO_2 does not alter the crystalline phases composition. Crystallization kinetics analysis shows ZrO_2 acts as heterogeneous nucleation centers, promoting diopside formation. For 2 μm and 50 nm ZrO_2, the crystallization activation energy increases with doping up to 30 wt% but decreases thereafter due to agglomeration-induced energy localization, whereas 200 nm ZrO_2 yields a continuous reduction, reflecting a balance between surface activity and dispersion stability. These findings provide insights for designing glass-composite sealants with optimized microstructures and improved performance in SOFC applications.

Received 14th November 2025
Accepted 28th January 2026

DOI: 10.1039/d5ra08813e

rsc.li/rsc-advances

1. Introduction

Solid Oxide Fuel Cells (SOFCs) are highly efficient and environmentally friendly energy conversion devices that enable direct chemical to electrical energy conversion without intermediate thermal processes. They are widely regarded as one of the most promising technologies to address the global energy shortage and environmental degradation, while meeting the urgent demand for sustainable energy development. Based on structural configuration, SOFC can be categorized into planar and tubular designs. Among them, planar SOFCs feature an all-solid-state structure that enables low manufacturing and design costs, facile modularity, and high scalability. This design offers higher power density and conversion efficiency, as well as lower electric resistance compared to other geometries.[1] Despite these advantages, planar SOFCs face several technical challenges, among which the development of reliable sealing materials is particularly critical.[2–5] Sealants ensure hermetic connections between adjacent cell components. During operation, SOFCs are exposed to harsh conditions, including prolonged high temperatures (600–1000 °C), mismatches in coefficients of thermal expansion (CTE) between different components, and atmospheres that may be oxidizing, reducing and humid. These factors impose stringent requirements on sealing materials.[6] An ideal sealant should meet several essential criteria:[7,8] (i) gas-tightness to prevent leakage of reactants; (ii) thermal expansion compatibility with adjoining components to minimize stress-induced cracking and sealing failure, (iii) chemical and structural stability to withstand thousands of thermal cycles without degradation, and (iv) adequate mechanical and electrical properties to ensure long-term stable operation.

To satisfy these requirements, different sealing strategies-compressive seals, compliant seals, and rigidly bonded seals-have been investigated.[7] Among these, glass and glass-ceramic seals have attracted the most attention, as they best meet the rigid sealing requirements of planar SOFCs.[9] Typically, glass seals are composed of network formers, network modifiers, and intermediate oxides, sometimes supplemented by additives.[10] By tailoring these constituents, sintering and crystallization behavior can be controlled to achieve the desired thermal and mechanical properties. Commonly used glass systems include alkaline earth silicate and borosilicate families, such as BaO–La_2O_3–Al_2O_3–B_2O_3–SiO_2, SrO–La_2O_3–Al_2O_3–B_2O_3–SiO_2, and MgO–CaO–Al_2O_3–SiO_2.[11] Recent studies have highlighted

[a]*Key Laboratory for Power Machinery and Engineering of M.O.E., School of Mechanical Engineering, Shanghai Jiao Tong University, Shanghai 200240, China. E-mail: tonyzhulei@sjtu.edu.cn*
[b]*College of Smart Energy, Shanghai Jiao Tong University, Shanghai 200240, China. E-mail: chaoma99@sjtu.edu.cn*

several key issues regarding the applications of seals in SOFCs.[12–15] Considering the choice of glass systems, different glass systems, however, present distinct limitations under specific conditions. For instance, borosilicate glasses suffer from B_2O_3 volatilization under humid reducing atmosphere, producing volatile $B_2(OH)_2$ and $B_2(OH)_3$ that impair sealing stability.[16] Phosphate glasses, with relatively weak networks, are unstable under SOFC operating conditions. P_2O_5 volatilization and its potential reaction with anodes may lead to formation of harmful secondary phases and undesirable CTE increases.[17] In contrast, silica-based glass systems offer greater stability.

Glass composite sealing, which combines pre-synthesized glass powders with inert ceramic fillers, provides a versatile route to optimize sealant performance.[18] Compared with solely modifying glass composition, the incorporation of filler particles with different types and morphologies can significantly influence the sintering and crystallization kinetics. Ceramic fillers can enhance viscosity, toughness, and thermal shock resistance of the sealant. Increased viscosity, in particular, restricts excessive viscous flow at operating temperature while still enabling crack healing procedure. Moreover, filler particles may facilitate controlled devitrification process, thereby reinforcing the glass matrix, improving chemical stability, and ensuring long-term performance.[19] Such regulation mitigates abrupt variations in the CTE, thereby improving interfacial bonding and enhancing the ability to absorb thermal stress.[20] Several studies have demonstrated the potential of glass composite seals. Sodium aluminosilicate (NAS) glass with MgO-fillers exhibits improved CTE matching and thermal cycling tolerance.[21] Silicate glass containing alkali/alkaline earth modifiers and 10%–30 wt% yttria-stabilized zirconia (YSZ) shows increased effective viscosity, as indicated by higher glass transition and softening temperatures, along with a reduced CTE.[22] Incorporating 20 wt% Al_2O_3 into a $BaO–CaO–B_2O_3–Al_2O_3–SiO_2$ glass effectively suppresses crystallization, strengthens the matrix, and contributes to both gas tightness and joint strength enhancement.[23] Despite extensive efforts in SOFC sealing research, the specific role of oxide additives from composite sealants in governing sintering and crystallization kinetics at high temperature remains insufficiently explored.

Achieving a sufficiently dense seal requires careful control of both the sintering and crystallization processes. During sintering, driven primarily by viscous flow, the seal must flow enough to heal pores and cracks and infiltrate adjacent components, but without excessive spreading. Subsequently, the precipitation of crystalline phases provides a rigid framework that stabilizes the geometry and enhances mechanical strength. However, if crystallization occurs prematurely during the early sintering phase, it can hinder densification, resulting in a porous sealing layer that compromises SOFC performance. Therefore, it is essential to study the sintering behavior of the glass to ensure that viscous flow is fully realized at the stage of maximum densification. Ideally, sintering should be completed before crystallization begins, thereby producing a dense and reliable sealing materials.

The onset of sintering typically occurs above the glass transition temperature. Prado *et al.*,[24] divide viscous flow driven sintering into three sequential stages: an initial 'Frenkel' (F) stage, a mixed 'Frenkel/Mackenzie-Shuttleworth' stage, and a final 'Mackenzie-Shuttleworth' (MS) stage. In the first stage, neck form between particles as small particles preferentially migrate into voids left by larger ones, accelerating their sintering; this process is well described by the Frenkel model.[25] Maximum shrinkage occurs when larger pores, originating from interparticle voids, are eliminated through viscous flow. The progressive reduction of these pore radii over time corresponds to the Mackenzie–Shuttleworth model of sintering.

Given the critical importance of sintering and crystallization process for achieving reliable hermetic sealing, it is essential to clarify the mechanistic role of the such oxide additives. In particular, ZrO_2, with its high toughness, chemical stability, and CTE closely matching that of YSZ, emerges as a particular suitable rigid filler for glass composites. Its addition not only reinforces the glass matrix and improves mechanical strength, but also regulates the crystallization behavior. Consequently, ZrO_2 is introduced primarily as a kinetic regulator and microstructural modifier. Its incorporation is intended to regulate the sintering and crystallization behavior of the glass composite sealant by influencing kinetic processes, heterogeneous nucleation, and microstructural evolution. Specifically, ZrO_2 serves two key functions: (i) it effectively broadens the sintering window and enhances localized densification,[18,26–28] and (ii) it acts as efficient heterogeneous nucleation centers within the glass matrix, thereby significantly reducing the crystallization activation energy and enabling controlled regulation of crystallization kinetics.[29,30] It is also important to clarify the distinction between the intrinsic incorporation of ZrO_2 into the glass composition and its introduction as a dispersed filler in composite sealants. When ZrO_2 is incorporated directly into the glass batch and melted together with other oxides, Zr^{4+} cations can be partially integrated into the glass network at the atomic scale. This integration modifies network connectivity, diffusion behavior, and crystallization pathways, as well as local coordination environments and the thermodynamic driving forces for crystallization. As a result, intrinsic incorporation typically exerts a more pronounced influence on glass structure and crystallization kinetics. In contrast, when ZrO_2 is introduced *via* a composite approach, it is presented as a physically dispersed secondary phase and does not participate directly in the formation of the glass network.[31] Under these conditions, the primary role of ZrO_2 is governed by interfacial interactions between the glass matrix and ceramic particles rather than by direct structural modification of the glass network. Consequently, the modification effect achieved through the composite approach is generally less pronounced than that obtained through direct compositional incorporation of ZrO_2, since the latter operates at the atomic scale, whereas the former is controlled mainly by interfacial and microstructural effects. Nevertheless, this kinetic–microstructural coupling remains essential for achieving reliable and hermetic sealing in high-temperature electrochemical devices, which constitutes the central scientific motivation of the present work. Therefore, a systematic kinetic investigation of the role of ZrO_2 in sintering and crystallization *via* the composite approach is critical for

optimizing microstructural evolution and ultimately improving the overall sealing performance.

Accordingly, the present work systematically investigates the effects of ZrO_2 particle size and concentration on the sintering and crystallization kinetics of silicate-based glass composite sealants. The study focuses on shrinkage behavior, sintering characteristic temperature, viscous flow modification, and crystalline phase formation of glass composite sealing with ZrO_2 addition. Special attention is given to elucidating the role of ZrO_2 fillers in tailoring microstructural evolution through sintering and crystallization kinetics modification, with the ultimate aim of providing insights into the design of glass composite sealants with optimized high-temperature performance for planar SOFCs.

2. Experimental

2.1. Materials and preparation

The base glass powder (MO-Al_2O_3–SiO_2 (M = Mg/Ca)) with an average grain size of $d_{50} = 38$ μm was supplied by Hebei Shahe Glass Co., Ltd, and is hereafter referred to as GC. The glass composition (molar fraction) is listed in Table S1. Commercial ZrO_2 powder (Macklin, 99.99%) with three particle sizes ($d_1 = 2$ μm, $d_2 = 200$ nm, $d_3 = 50$ nm) were used as rigid fillers. Glass composite powders were prepared by thoroughly wet mixed GC with ZrO_2 particles of different sizes at loading of 10, 20, 30, and 40 wt%, denoted as GCZ10, GCZ20, GCZ30, GCZ40, respectively. The mixtures were ball milled for 4 hours in ethanol using a pendulum vibration ball mill (400 rpm) with zirconia beads of three diameters: 10 mm, 8 mm, and 5 mm, in a ratio of 12 : 25 : 20. Beads, powder, and ethanol each occupied one-third of the nylon jar volume. Prior to milling, both glass and ZrO_2 powders were ultrasonically dispersed to minimize agglomeration. The suspensions were dried for 24 hours, granulated in a mortar, and sieved through a 200-mesh stainless steel screen to obtain the final composite powders.

The powders were uniaxially cold-pressed (80 MPa, 5 minutes) into different shapes depending on subsequent analysis. For sintering test, cylinders (Φ 5 mm × 5 mm) were prepared; for porosity and XRD analysis, pellets with a diameter of 10 mm were fabricated; for CTE measurement, rectangular bars with dimensions of 6.5 mm × 20 mm were prepared. Green pellets and bars were subjected to multi-step heat treatment: first at 750 °C or 800 °C (corresponding to the temperature of maximum shrinkage rate, obtained from the first derivative of dilatometry curves) for 2 hours, then at 900 °C for 1 hour, and finally at 850 °C for 4 hours or 20 hours. Heating and cooling rates were fixed at 2 °C min^{-1}. The sintered pellets were ground with SiC paper and polished with cloth for subsequent characterization. The sintered bars were also carefully ground with SiC paper at both ends to obtain flat and parallel surfaces.

2.2. Thermal characterization

Sintering characteristic temperatures, including the first shrinkage temperature (T_{FS}), maximum shrinkage temperature (T_{MS}), and softening temperature (T_D), were determined by dilatometry (DIL 402 Expedis Select, Netzsch, Germany) using pressed cylinders, heated from 25 °C to 1100 °C at 5 °C min^{-1}. Differential scanning calorimetry (DSC 404 F3, Netzsch, Germany) was performed using platinum crucibles under flowing air at 25∼1200 °C, at heating rates of 5, 10, 15, and 20 °C min^{-1}. Calcined α-Al_2O_3 (1200 °C) was used as an inert reference. The glass transition temperature (T_g) and crystallization peak temperature (T_p) were extracted from the DSC curves. The thermal expansion behavior analysis was carried out on sintered bars by using the dilatometer (DIL 402 Expedis Select, Netzsch, Germany) under a controlled heating rate of 5 °C min^{-1}. Then the obtained curves were imported into the integrated analysis software (Netzsch Proteus Analysis) to calculate the average CTE (α) for each sample within the temperature range of 50 to 900 °C.

2.3. Crystallization analysis

X-ray diffraction (XRD, Mini Flex 600, Rigaku, Japan) with Cu-Kα radiation (40 kV, 15 mA) was employed to analyze polished sintered pellets. Data were collected at 6° min^{-1} in the 2θ range of 10–80°. Crystalline phases were identified using MIDI Jade 9 software and the PDF-4 database (International Centre for Diffraction Data – ICDD, Newtown Square, PA).

2.4. Microstructure morphology characterization

Microstructures of polished pellets were observed by scanning electron microscopy (SEM, Zeiss, Germany) at 15 kV. Prior to imaging, samples were sputter-coated with a thin gold layer. Elemental mapping was performed using energy dispersion X-ray spectroscopy (EDS, Quantax, Bruker, Germany) to assess the distribution of ZrO_2 inclusions and crystalline phases. Porosity values were quantified using ImageJ software, applying the same threshold to all samples for consistency.

3. Results and discussion

3.1. Sintering analysis

The sintering curves of the glass and glass composite powders, obtained by dilatometry, are presented in Fig. S1–S4. The curves were analyzed by taking their first derivatives to identify

Table 1 Characteristic temperature (T_{FS}, T_{MS}, T_D) of GC and GCZ obtained from the sintering curve

Sample	T_{FS} (°C)			T_{MS} (°C)			T_D (°C)		
GC	680.9			754.7			814.7		
	2 μm			200 nm			50 nm		
Sample	T_{FS} (°C)	T_{MS} (°C)	T_D (°C)	T_{FS} (°C)	T_{MS} (°C)	T_D (°C)	T_{FS} (°C)	T_{MS} (°C)	T_D (°C)
GCZ10	663.8	750.3	814.0	665.5	752.0	822.6	667.2	753.2	817.1
GCZ20	678.4	762.1	825.8	667.1	773.9	836.2	669.2	745.6	826.5
GCZ30	674.3	767.6	829.1	658.0	793.4	857.8	659.2	765.7	839.3
GCZ40	665.6	807.2	857.3	662.0	813.2	860.1	667.2	760.3	797.0

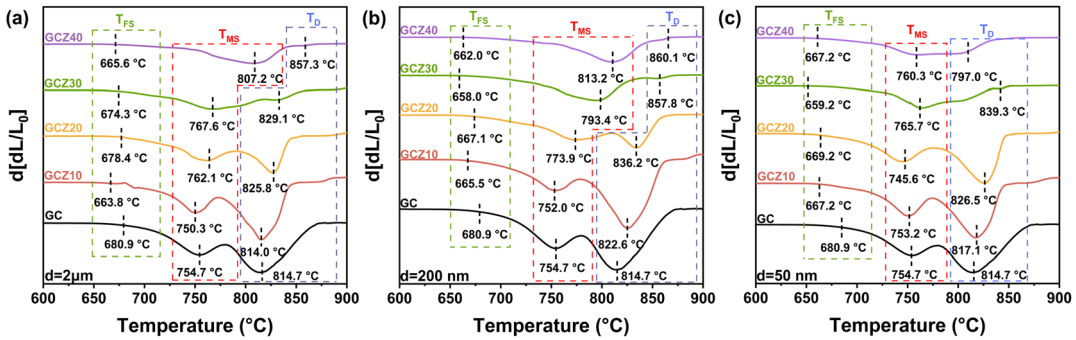

Fig. 1 Comparison of the first derivative curves of the sintering curves for different mass fraction of (a) 2 μm ZrO_2, (b) 200 nm ZrO_2 and (c) 50 nm ZrO_2.

characteristic points.[32] Two characteristic peaks were observed: T_{MS} (the first peak) and T_D (the second peak). T_{FS} is defined as the temperature at which measurable shrinkage of the sample first occurs.[33–35] Accordingly, the zero crossing of the first derivative curves are referred to as T_{FS} values. All sintering characteristic temperatures (T_{FS}, T_{MS} and T_D) are summarized in Table 1. For the pristine glass (GC), the densification rate at T_D is higher than that at T_{MS}. With the incorporation of ZrO_2, the first shrinkage temperature T_{FS} decreases, indicating an earlier onset of sintering. Meanwhile, the shrinkage rate at T_{MS} progressively surpasses that at T_D, and this effect becomes more pronounced as the ZrO_2 content increases. At 30 wt% ZrO_2, the

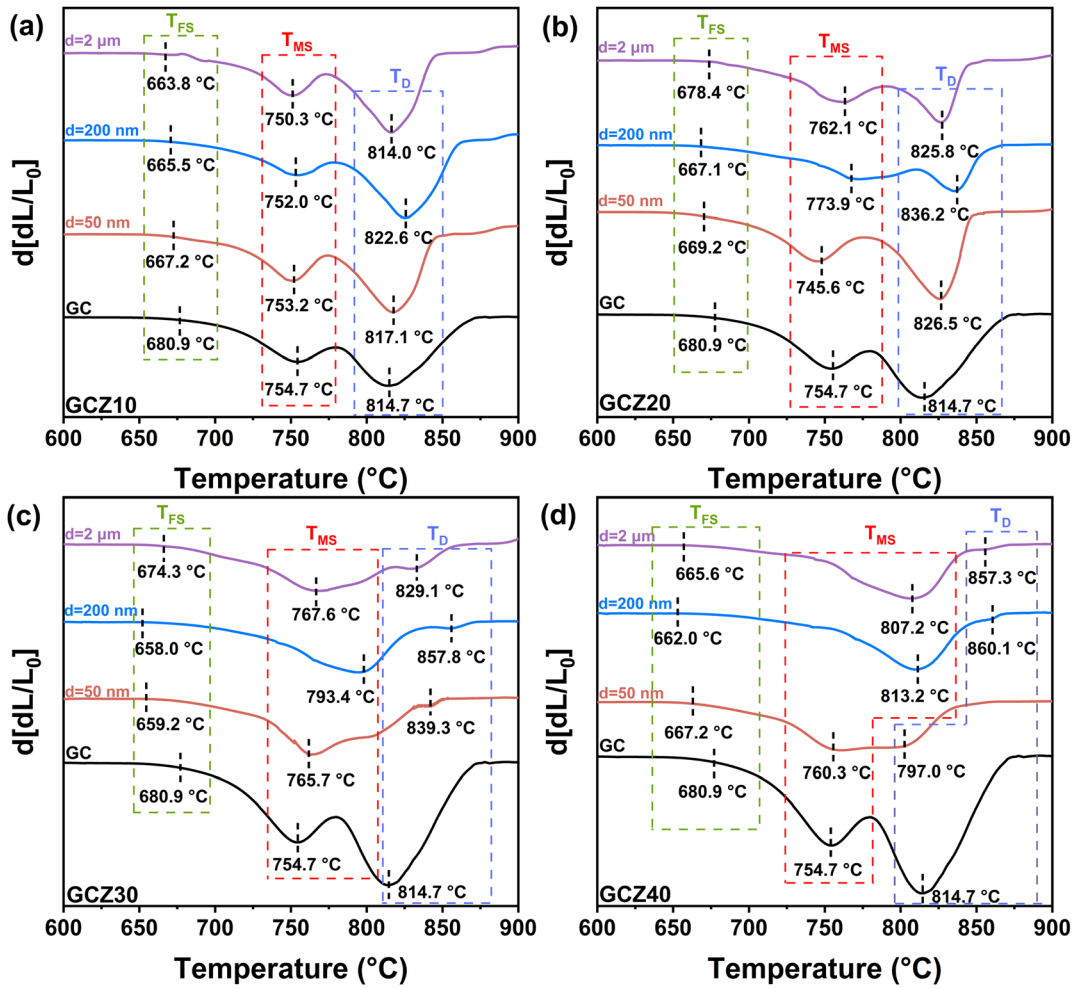

Fig. 2 Comparison of the first derivative curves of the sintering curves for different particle sizes of (a) GCZ10, (b) GCZ20, (c) GCZ30 and (d) GCZ40 samples.

optimum sintering temperature shifts completely from T_D to T_{MS}, suggesting that the densification control process has transitioned from the $T_{MS}-T_D$ segment to the $T_{FS}-T_{MS}$ segment. This shift enables sintering to occur earlier, reducing overlap with crystallization and thereby avoiding incomplete densification. Comparison of the first derivative curves for different ZrO_2 contents and particle sizes are shown in Fig. 1 and Fig. 2, with characteristic temperature labeled. The incorporation of ZrO_2 regardless of particle size, significantly influences the sintering behavior: T_{FS} decreases while T_{MS} increases, thereby extending the overall sintering stage. This effect intensifies with increasing ZrO_2 content. In addition, T_D is elevated, implying enhanced resistance to deformation at high temperatures.

The influence of ZrO_2 particle size on sintering is depicted in Fig. 2. At a fixed loading, all three particle sizes promote an elongation of the sintering stage, though the effect does not follow a simple linear trend. In all cases, the shrinkage rate below T_{MS} exceeds that at T_D, indicating improved densification prior to softening. Notably, 200 nm ZrO_2 exhibits the strongest extension effect between T_{FS} and T_{MS}. As a result, composites containing 200 nm particles display the highest T_D, corresponding to the greatest resistance to viscous flow and deformation at elevated temperatures.

Fig. S5 and S6 provide further insight into the influence of inert ZrO_2 fillers on the characteristic temperatures and shrinkage behavior of GC. As shown in Fig. S5, the temperature span between T_{FS} and T_{MS} progressively widens with increasing ZrO_2 content, indicating an extended window for densification prior to $T_{MS}-T_D$ segment. Namely, sintering becomes more predominant at $T_{FS}-T_{MS}$ segment. Concurrently, T_D rises significantly, while the overall shrinkage rate decreases. This inverse relationship suggests that ZrO_2 effectively suppresses excessive deformation at elevated temperatures, thereby enhancing the dimensional stability of the sealing material. Taken together with the sintering analysis, these results indicate that the incorporation of ZrO_2 shifts sintering toward an earlier yet more moderate stage, improving densification without compromising structural integrity.

The effect of particle size is highlighted in Fig. S6. At comparable loading, 200 nm ZrO_2 particles exert the strongest influence on sintering behavior, yielding the highest T_D and the lowest shrinkage values among the three particle sizes. This indicates that fillers of this size optimize the balance between particle dispersion and structural reinforcement, resulting in enhanced stiffness and reduced susceptibility to viscous flow-induced deformation. The pronounced effect of the 200 nm particles underscores the critical role of filler size in tailoring the sintering kinetics and mechanical stability of glass composite sealants.

The DSC plots of the investigated samples at different heating rates are shown in Fig. S7–S10. To evaluate the crystallization kinetics, DSC tests were carried out under multiple heating rates. During heating, the initial endothermic signal-manifested as a slight inflection in the DSC curves-corresponds to the glass transition temperature T_g. With further temperature increase, an exothermic peak emerges after

Table 2 Characteristic temperature (T_g and T_p) of GC and GCZ obtained from the DSC curve

Sample	T_g (°C)					T_p (°C)
GC			629.3			840.1
	2 μm		200 nm		50 nm	
Sample	T_g (°C)	T_p (°C)	T_g (°C)	T_p (°C)	T_g (°C)	T_p (°C)
GCZ10	630.9	838.8	632.4	842.5	630.6	840.4
GCZ20	635.4	844.0	637.8	844.3	634.7	840.3
GCZ30	636.5	836.6	640.6	847.6	638.4	839.3
GCZ40	633.5	847.7	636.0	848.6	633.0	847.1

T_g, attributable to the formation of crystalline phases; the maximum of this peak defines the crystallization temperature (T_p) of the samples.

Notably, the DSC curves of the ZrO_2-containing composite sealants exhibit a weak exothermic peak at approximately 300 °C. This feature is attributed to atomic rearrangement occurring at the glass–ZrO_2 interfacial region during heating. Such process reduces the excess interfacial energy introduced by ZrO_2 incorporation and facilitates a more homogeneous dispersion of the ZrO_2 particles within the glass network. As the composite system evolves from a high-energy configuration toward a thermodynamically more stable state, the associated enthalpy decrease is released in the form of heat, leading to the observed low-temperature exothermic signal. Characteristic temperatures acquired from the DSC curve (heating rate 5 °C min^{-1}) are summarized in Table 2. As the heating rate increases, both characteristic temperatures shift to higher values.[36] The results reveal that the addition of ZrO_2 leads to an increase in T_g, indicating an enhancement of the glass network structure under high temperature.[37] The variation of T_p is closely related to the crystallization process, which will be analyzed in detail in the following section on crystallization kinetics. Based on the liquid theory proposed by Mott and Gurney,[38] the following relationship exists between pseudo-critical temperature (T_k) and the absolute melting point (T_m):

$$\frac{T_k}{T_m} = \frac{2}{3} \quad (1)$$

It is demonstrated that this relation also applies to glass-ceramic systems.[39] Substituting T_k with T_g and T_m with the liquidus temperature (T_l) of glass, the expression becomes:

$$\frac{T_g}{T_l} = \frac{2}{3} \quad (2)$$

Thus, T_l for each sample can be calculated directly from the measured T_g values obtained from DSC. At this stage, T_g, T_D, and T_l (expressed in kelvin) are determined. The viscosity (η) at these characteristic temperatures is regarded as a constant ($\eta_g = 13.6$ dPa s, $\eta_D = 11.6$ dPa s, $\eta_l = 4$ dPa s), independent of glass composition.[40] To describe the viscosity–temperature

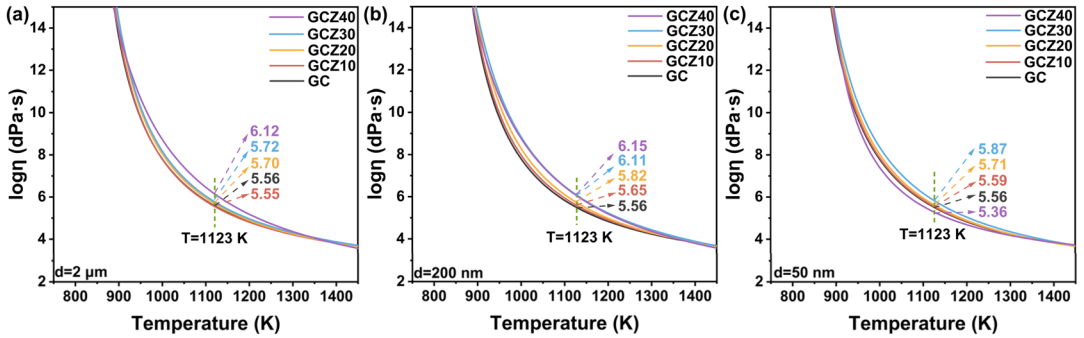

Fig. 3 Viscosity–Temperature relationship for different mass fraction of (a) 2 μm ZrO_2, (b) 200 nm ZrO_2 and (c) 50 nm ZrO_2.

relationship, the Vogel–Fulcher–Tammann (VFT) equation was employed (eqn. (3)):[41,42]

$$\log \eta = A + \frac{B}{T - T_0} \tag{3}$$

where A, B and T_0 are fitting constants. By substituting the characteristic temperatures and their corresponding viscosity values into eqn (3), the coupled equations can be solved to determine A, B, and T_0, thereby establishing the viscosity-temperature dependence of each composition. It should be noted, however, that due to the inherent limitations of the VFT model,[43] the viscosity curves presented here are intended for comparative analysis and reference, rather than as precise quantitative predictions over a broad temperature range.

Fig. 3 and Fig. 4 illustrate the viscosity–temperature relationships of the composite sealants after doping with ZrO_2 of different concentrations and particle sizes. To elucidate the microscopic mechanisms underlying the influence of ZrO_2 on viscosity, the sintering behavior of the composites near their characteristic sintering temperatures was investigated, with

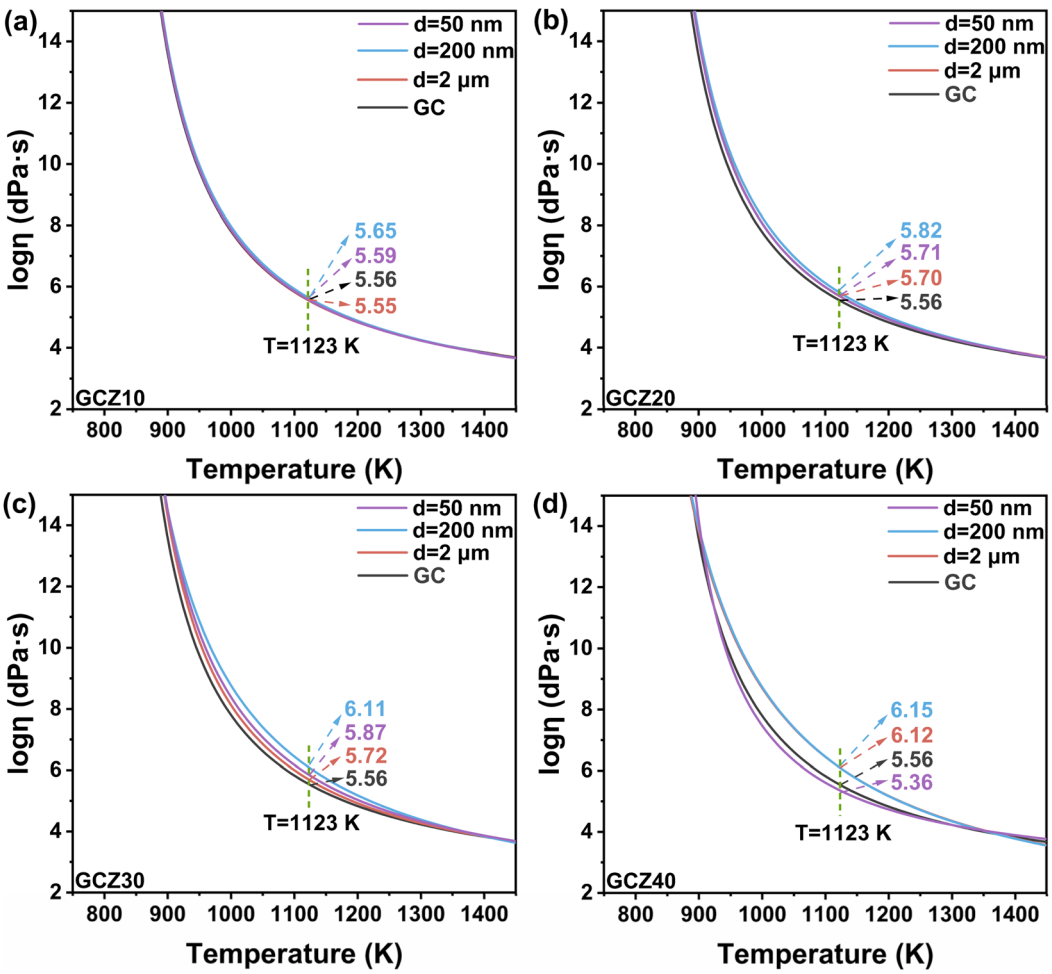

Fig. 4 Viscosity–Temperature relationship for different particle sizes of (a) GCZ10, (b) GCZ20, (c) GCZ30 and (d) GCZ40 samples.

particular attention to changes in the glass network structure. Green pellets were prepared by uniaxial pressing and subsequently heated to 700 °C, 750 °C, and 800 °C with a dwelling time of 2 hours at each target temperature. The samples were then cooled under identical conditions, ground, polished, and examined *via* scanning electron microscopy (SEM). Porosity was quantified by binarizing SEM images using ImageJ software. The results are summarized in Fig. S11 and S12, with representative SEM micrographs provided in the SI (Fig. S31–S43). These results confirm that maintaining the glass composites (GC and GCZ) close to their maximum sintering rate temperatures is essential to achieve low porosity and sufficient densification before the onset of crystallization.

As shown in Fig. 3, the viscosity of the composite sealants is varied at the SOFC operating temperature ($T = 1123$K) by ZrO_2 content. For both 2 μm and 200 nm ZrO_2 fillers, the viscosity is consistently higher than that of the undoped glass ($\eta = 5.56$ dPa s), and increases monotonically with ZrO_2 mass fraction. This indicates that ZrO_2 reduces the flowability of the composite and enhances its resistance to macroscopic deformation, consistent with the reduced shrinkage observed in Fig. S5 and S6. SEM analysis further reveals that ZrO_2 particles are preferentially located at the boundaries of the amorphous regions, segmenting the continuous glass network into discrete microdomains. With increasing filler content, the particle concentration progressively fills the free volume within the network, thereby raising the energy barrier for viscous flow. Consequently, the composite viscosity increases. However, the higher viscosity simultaneously hinders densification during sintering, resulting in higher porosity.

Interestingly, a non-monotonic behavior is observed for 50 nm ZrO_2 fillers. The viscosity increases with ZrO_2 loading up to 30 wt%, but decreases sharply beyond this threshold. SEM images (Fig. S56) confirm that the occurrence of severe particle agglomeration at high loading. Owing to their high specific surface area and associated surface energy, the nanoparticles tend to form large, loosely bonded soft agglomerates rather than remaining homogeneously dispersed. These agglomerates reduce the effective surface area for ZrO_2-glass interactions and disrupt the continuity of the reinforcement network, promoting localized slip or deformation under shear stress. As a result, the resistance to viscous flow is compromised, leading to reduced viscosity.

The effect of particle sizes is summarized in Fig. 4. Across the doping range of 10–40 wt%, the 200 nm ZrO_2 fillers consistently yield the highest viscosity. Compared to 2 μm particles, the 200 nm particles offer a larger specific surface area, which strengthens particle–matrix interactions and interfacial friction. This effectively restricts glass flow and promotes the development of a robust, interconnected structure. SEM observations show that 2 μm ZrO_2 particles tend to aggregate into larger clusters (as presented in Fig. 5c), whereas 200 nm particles remain more uniformly distributed within the glass phase (as presented in Fig. 5h), ultimately forming a rigid three-dimensional percolation framework (RPF).[44] This RPF significantly impedes macroscopic viscous flow, resulting in the marked overall viscosity increase.

Although inert fillers generally increase viscosity and reduce flowability-conditions unfavorable for pore elimination-the formation of an RPF structure alters the local sintering dynamics. The web-like distribution of fine ZrO_2 particles partitions the amorphous phase into confined regions, enhancing resistance to global viscous flow while simultaneously lowering the energy barrier for local viscous rearrangements. This facilitates more effective sintering within each microdomain.[44] During the initial stage of sintering, the RPF promotes the development of multiple healing 'anchor points', and as sintering proceeds, these radial cracks gradually close in a segment-by-segment fashion, ultimately leading to reduced porosity (Fig. S12).[44] Thus, the 200 nm fillers achieve lower porosity compared to other particle sizes.

SEM observation reveals isolated spherical closed pores within the composite sealants, without forming continuous channels through the materials. These closed pores do not provide continuous leakage pathways, promising the hermetic sealing performance.

When the ZrO_2 particle size is further reduced to 50 nm, the propensity for agglomeration increases, particularly at higher loading. This undermines particle dispersion and compromises the structural uniformity of the composite, thereby diminishing mechanical integrity. Overall, reducing ZrO_2 particle size from the micrometer to nanometer scale induces a non-monotonic viscosity trend—initially rising and subsequently falling. This reflects a competition between two effects: the enhanced interfacial interactions associated with increased surface area (beneficial), and the agglomeration tendency of nanoscale fillers (detrimental).

According to the study by Mahedevan *et al.*,[45] the glass transition temperature values of both GC and GCZ were employed to calculate the activation energy associated with viscous flow. This approach enables an evaluation of the viscous flow behavior of the glass and glass–ceramic composite sealants from an energy perspective. Two parameters were introduced to characterize this behavior: the activation energy for viscous flow (E_η) and the fragility index (F). The former reflects the resistance of the material to viscous deformation, while the latter provides insight into the stability of its internal structure. The activation energy for viscous flow was determined using the Kissinger equation:[46,47]

$$\ln\left(\frac{\alpha}{T_g^2}\right) = -\frac{E_\eta}{RT_g} + \text{constant} \quad (4)$$

where α denotes the heating rate, and R is the universal gas constant. A linear relationship is obtained by plotting $\ln(\alpha/T_g^2)$ against $1/T_g$, with the slope of the fitted line yielding the activation energy. The fragility index (F) was calculated using the eqn (5):[48–50]

$$F = \frac{E_\eta}{RT_g \ln 10} \quad (5)$$

This parameter serves as a measure of the material's fragility, indicating its deviation from the ideal Arrhenius behavior near the glass transition.

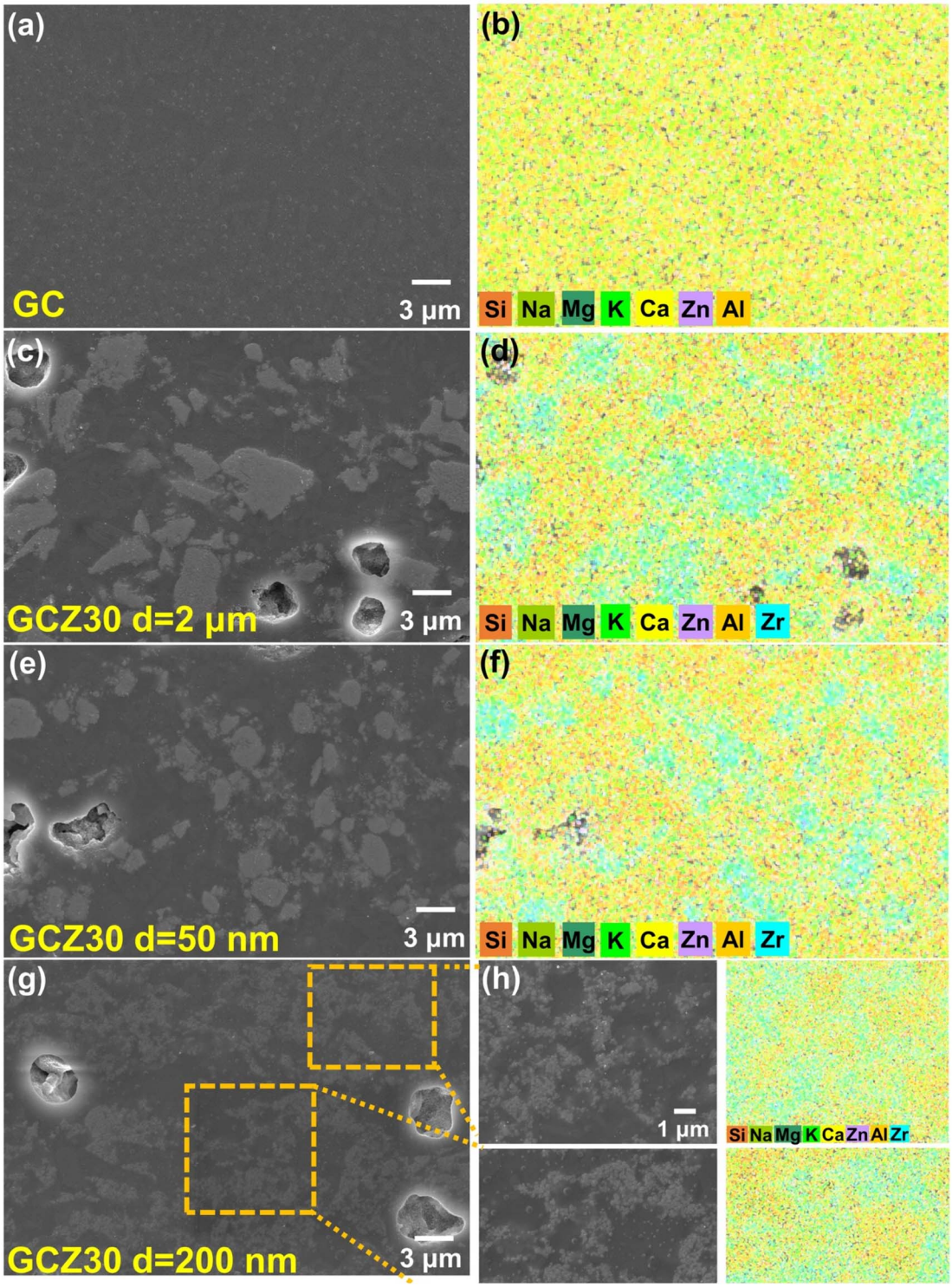

Fig. 5 (a) SEM morphology of GC, (b) elemental distribution of GC, (c) SEM morphology of GCZ30, $d = 2$ μm sample, (d) elemental distribution of GCZ30, $d = 2$ μm sample, (e) SEM morphology of GCZ30, $d = 50$ nm sample, (f) elemental distribution of GCZ30, $d = 50$ nm sample, (g) SEM morphology of GCZ30, $d = 200$ nm sample and (h) SEM morphology of RPF structure and elemental distribution in GCZ30, $d = 200$ nm sample.

The results are presented in Fig. S13 and S14 and summarized in Table 3. The relationship between the activation energy for viscous flow (E_η) and ZrO_2 content shows a non-linear trend, first increasing and then decreasing. A maximum in E_η is observed at 30 wt% ZrO_2, corresponding to the highest resistance to viscous flow and a marked increase in viscosity. Beyond this composition, E_η decreases; however, the overall flowability of the material does not improve. This behavior is attributed to the excessive ZrO_2 particles occupying the free volume of the glass network, which limits the mobility of the

Table 3 The activation energy for viscous flow (E_η) and relative fragility index F of GC and GCZ samples

Sample	E_η (kJ mol^{-1})	F
GC	376.44	21.79

	2 μm		200 nm		50 nm	
Sample	E_η (kJ mol^{-1})	F	E_η (kJ mol^{-1})	F	E_η (kJ mol^{-1})	F
GCZ10	394.16	22.77	417.12	24.06	397.96	22.95
GCZ20	474.08	27.26	497.69	28.54	462.58	26.62
GCZ30	502.70	28.87	537.01	30.70	526.84	30.19
GCZ40	456.67	26.31	498.65	28.65	469.71	27.08

viscous glass phase even when the activation barrier is reduced. Among the different particle sizes at a fixed ZrO_2 content, 200 nm ZrO_2 exhibits the strongest effect in enhancing E_η. As previously discussed, this arises from the formation of the RPF structure along the boundaries of the glass region. The RPF effectively partitions the amorphous glass matrix, thereby restricting macroscopic viscous flow.[28,51] In contrast, ZrO_2 particles of larger size (2 μm) or smaller size (50 nm) tend to aggregate into clusters, leading to weaker interfacial interactions with the glass phase and, consequently, a reduced ability to constrain flow behavior. These findings emphasize the importance of T_g in interpreting the thermal response and flow characteristics of the composites. The inclusion of inert fillers modifies the glass sintering process at the microscopic energy-barrier level by altering the activation energy of viscous flow, thereby influencing the overall sintering dynamics.

The relative fragility index F further elucidates the thermal behavior of the composites. Defined as a dimensionless parameter describing how relaxation time decreases with increasing temperatures near the T_g, F shows a notable increase upon ZrO_2 incorporation.

This indicates that the relaxation dynamics of the modified composite become more sensitive to temperature fluctuations near the glass transition. As a results, the decline in relaxation time becomes steeper, suggesting a more abrupt structural response and a tendency toward brittleness. This trade-off implies that improved sintering resistance may come at the cost of reduced thermal stability. Nevertheless, the calculated fragility indices for all system remain well below 200. According to Vilgis,[52] glass-forming liquids with Arrhenius-type relaxation times are classified as strong, and typically exhibit low fragility indices ($F \approx 16$), while fragile glass formers approach values near 200.[53,54] Thus, the ZrO_2 modified glass composite system can still be classified as a relatively strong glass former, capable of forming a thermally stable glass phase. These results highlight that optimizing the sealing performance of glass-ceramic composites requires balancing sintering characteristics with thermomechanical reliability, particularly under high-temperature operating conditions.

3.2. Crystallization analysis

The XRD patterns of the glass and glass ceramic composite sealants after heat treatment at 850 °C for 4 h and 20 h are shown in Fig. 6, 7 and S15-16. Only two crystalline phases were detected: diopside ($Ca(Mg_{0.7}Al_{0.3})(Si_{1.7}Al_{0.3})O_6$, PDF: 97-006-2547) and zirconia (ZrO_2, PDF: 97-008-0048). No additional phases were observed, indicating that the crystallization behavior of the system is both stable and well-controlled under the investigated thermal conditions.

With increasing ZrO_2 content, the diffraction peaks of zirconia gradually intensified, reflecting enrichment of the zirconia phase. Within the range of compositions and particle size studied, neither the ZrO_2 concentration nor its particle size influenced the type of crystalline phases formed, even with prolonged isothermal holding up to 20 hours. These results highlight the excellent phase stability of the ZrO_2-modified composite sealants. The inert character of ZrO_2 prevents significant alterations to the crystallization pathway of the glass matrix, thereby avoiding excessive crystallization that could otherwise generate thermal stresses or mismatch in the CTE. Consequently, the system demonstrates strong potential for stable long-term performance in high temperature environments. Once the composite sealants have achieved sufficient sintering and densification, understanding their crystallization behavior becomes essential.

This section aims to clarify the regulatory role of inert ZrO_2 fillers on crystallization kinetics. To quantitatively assess the influence of these fillers, the crystallization activation energy (E_c) and Avrami exponent (n) were employed as descriptors of

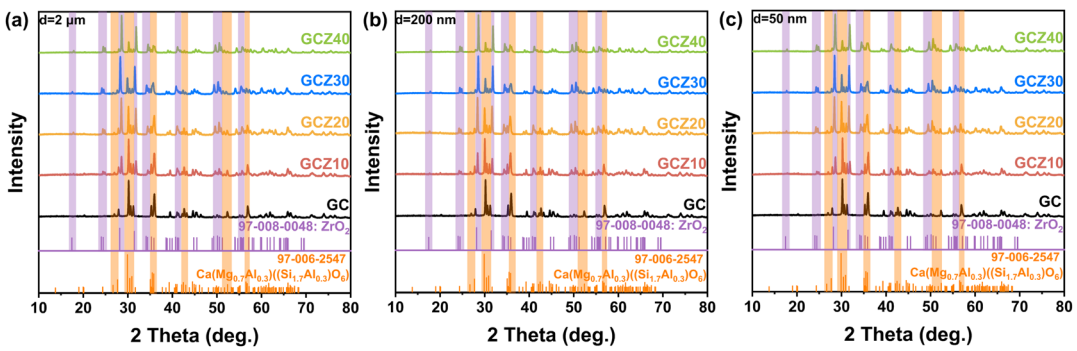

Fig. 6 XRD patterns for different mass fraction of (a) 2 μm ZrO_2, (b) 200 nm ZrO_2 and (c) 50 nm ZrO_2 after heat-treatment for 4 hours.

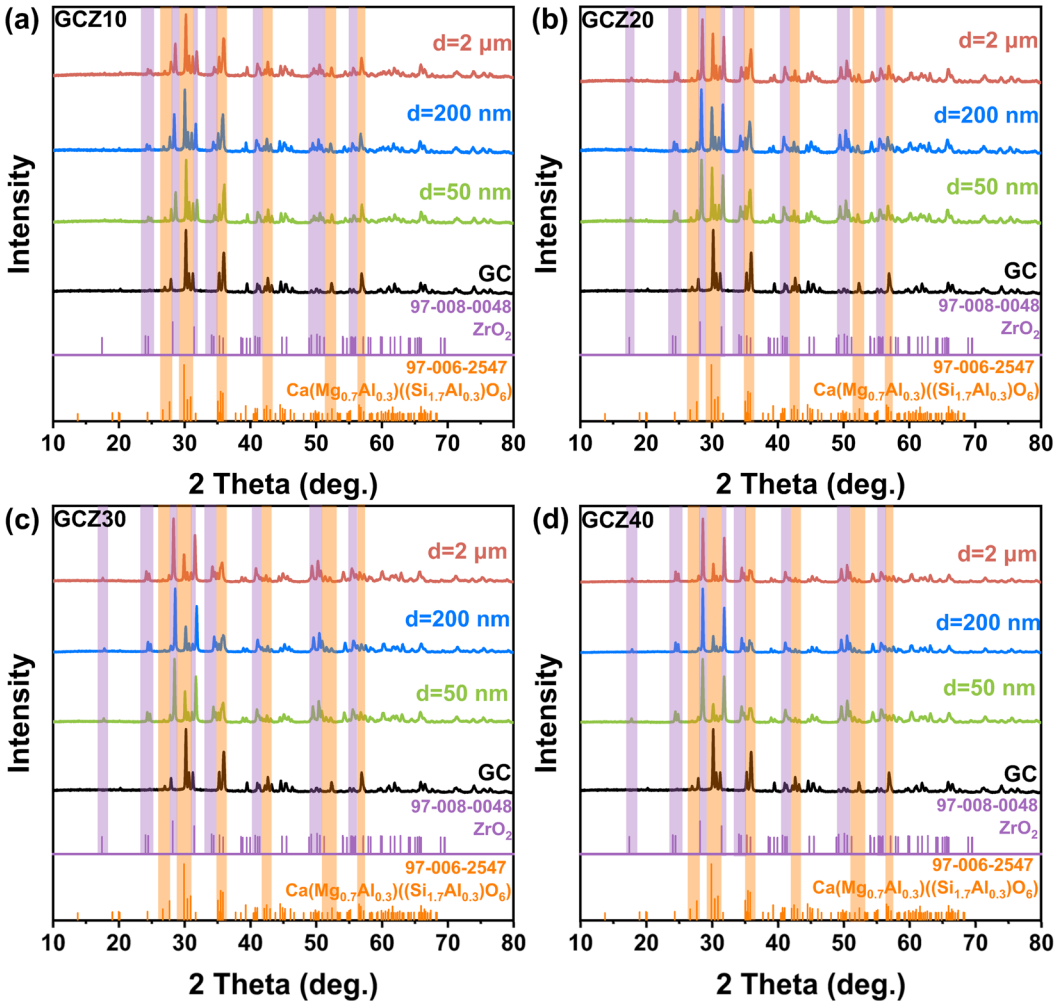

Fig. 7 XRD patterns for different particle sizes of (a) GCZ10, (b) GCZ20, (c) GCZ30 and (d) GCZ40 samples after heat-treatment for 4 hours.

crystallization rate and mechanism. The activation energy was determined using three widely adopted kinetic models: Kissinger, Augis–Bennett, and Ozawa. These calculations were based on the peak crystallization temperature (T_p) values derived from DSC measurements. Owing to inherent theoretical differences among the models, variations in the calculated activation energies are expected.

The Kissinger model, a classical method for non-isothermal crystallization, is expressed as:[47,55]

$$\ln\left(\frac{\alpha}{T_p^2}\right) = -\frac{E_c}{RT_p} + \text{constant} \quad (6)$$

where α is the heating rate.

The Augis–Bennett model modifies the Kissinger approach as follows:[56]

$$\ln\left(\frac{\alpha}{T_p - T_0}\right) = -\frac{E_c}{RT_p} + \ln K_0 \quad (7)$$

where T_0 is a fixed reference temperature of 300 K, and K_0 is the frequency factor, representing the number of attempts per second for nuclei to overcome the crystallization barrier.

The Ozawa model assumes that the degree of crystallization is independent of heating rate and is expressed as:[57]

$$\ln \alpha = -\frac{E_c}{RT_p} + \text{constant} \quad (8)$$

All three models can be generalized as a linear relationship between $\ln(\alpha/(T_p - T_0)^n)$ and $1/T_p$, with the values of n and T_0 depending on the chosen model: Kissinger ($n = 2$, $T_0 = 0$), Augis–Bennett ($n = 1$, $T_0 = 300$), and Ozawa ($n = 0$, $T_0 = 0$). By plotting $\ln(\alpha/(T_p - T_0)^n)$ against $1/T_p$ and applying linear fitting (Fig. S17–S20), the slope of the fitted line corresponds to the crystallization activation energy.

For the non-isothermal crystallization process, the volume fraction of the crystallized phase χ_T at a given temperature T can be expressed as:[58,59]

$$\chi_T = \int_{T_x}^{T} C(T)\mathrm{d}T \Big/ \int_{T_x}^{T_f} C(T)\mathrm{d}T \quad (9)$$

where C(T) is the exothermic intensity at temperature T, obtained from the DSC curve. The onset T_x and completion T_f temperature mark the boundaries of the crystallization process. Thus, χ_T represents the fraction of the exothermic peak area integrated from T_x to T, relative to the total area under the entire crystallization peak (Fig. S21–S25). This provides a quantitative description of crystallization progression as a function of temperature at various heating rates. Geometrically, as illustrated in the figure, this corresponds to the ratio of the area under the exothermic peak between T_x and a given temperature T to the total area under the entire crystallization peak in the DSC curve.[60]

The Avrami parameter, often referred to as the crystallization kinetic index, is a dimensionless quantity that provides insight into the crystallization mechanism by reflecting both nucleation behavior and crystal growth characteristics. Analysis of the DSC profiles for investigated sample reveals that increasing the heating rate results in a larger internal temperature gradient. This condition suppresses the formation of crystalline nuclei while retaining a greater fraction of the uncrystallized glassy phase, ultimately shifting the crystallization peak temperature T_p to higher values. In other words, the systematic shift of T_p toward higher values with increasing heating rates is consistent with the characteristic behavior of non-isothermal crystallization kinetics, indicating that under more rapid heating conditions, higher temperatures are required to supply sufficient thermal energy to overcome the activation barrier for crystallization and to initiate the crystallization process effectively.[61–63] Under these conditions, the calculated Avrami parameters and their corresponding crystallization mechanisms are summarized in Table 4.[64] The Avrami parameter can be determined using the Ozawa equation:[65]

$$-n = \left(\frac{d\ \ln[-\ln(1-\chi)]}{d\ \ln\ \alpha}\right)_T \tag{10}$$

where χ represents the volume fraction of crystallized phase at a given temperature T, as obtained from eqn (9). To evaluate the Avrami parameter, five evenly distributed temperatures within the crystallization range (between T_x and T_f) were selected for each sample. At these temperatures, the values of χ were calculated at different heating rates. Subsequently, based on eqn (10), plots of $\ln[-\ln(1-\chi)]$ *versus* $\ln\alpha$ were constructed for each selected temperature, and linear fitting was performed (Fig. S26–S30). The slope of the fitted line at each temperature corresponds to the Avrami parameter. Finally, the average Avrami parameter $\langle n\rangle$ for each sample was obtained by calculating the arithmetic mean of the five individual n values. The crystallization activation energy E_c and the corresponding average Avrami parameter $\langle n\rangle$ for each sample are summarized in Table 5 and Table 6. The results show that the average Avrami parameter $\langle n\rangle$ for the unmodified glass-ceramic (GC) sample is approximately 2.0. As summarized in Table 4, this value corresponds to a two-dimensional crystal growth mechanism. Upon incorporation of ZrO_2 particles, $\langle n\rangle$ increases slightly, falling within the range of 2–3, which indicates a gradual transition of the crystallization mode from two-dimensional toward three-dimensional growth. An increase in the Avrami index reflects a tendency toward faster or multidimensional crystal growth, implying an enhanced crystallization capability of the glass.[64,66]

Further analysis of the E_c indicates that the addition of ZrO_2 particles, regardless of their concentration or particle size, consistently reduces the energy barrier for crystallization,

Table 4 Numerical values for Avrami parameter n used in the determination of activation energies for crystallization

Crystallization mechanism	Avrami parameter n
Bulk crystallization with an increasing number of nuclei (*i.e.* an as-quenched sample with the number of nuclei inversely proportional to the heating rate)	
Three-dimensional growth of crystals	4
Two-dimensional growth of crystals	3
One-dimensional growth of crystals	2
Surface crystallization	1

Table 5 The crystallization activation energy E_c of GC and GCZ samples calculated in three models (Kissinger model, Augis-Bennett model, and Ozawa model)[a]

	E_c (kJ mol^{-1}) Model								
Sample	Kissinger			Model Augis-Bennett					Ozawa
GC	349.51			355.54					368.34
	E_c (kJ mol^{-1}) Model								
	2 μm			200 nm			50 nm		
Sample	K	A-B	O	K	A-B	O	K	A-B	O
GCZ10	312.04	318.07	330.88	323.31	329.37	342.21	317.51	323.55	336.38
GCZ20	321.17	327.25	340.10	313.35	319.44	332.29	308.37	314.42	327.25
GCZ30	336.69	342.69	355.47	310.41	316.53	329.41	346.76	353.78	365.58
GCZ40	301.85	307.97	320.86	308.75	314.88	327.78	311.80	317.91	330.79

[a] (Note: 'K' refers to Kissinger model, 'A-B' refers to Augis-Bennett model, 'O' refers to Ozawa model.).

Table 6 The average Avrami parameter n of GC and GCZ samples calculated in eqn (10)

Sample			Average Avrami parameter $\langle n \rangle$
GC			2.0
	2 μm	200 nm	50 nm
Sample	$\langle n \rangle$	$\langle n \rangle$	$\langle n \rangle$
GCZ10	2.1	2.2	2.4
GCZ20	2.4	2.2	2.3
GCZ30	2.0	2.4	2.6
GCZ40	2.9	2.6	2.5

thereby facilitating crystal growth. This conclusion is corroborated by backscattered electron (BSE) imaging (Fig. S44–S56), which shows that the needle-shaped diopside phase (gray regions) preferentially nucleates and grows around ZrO_2 particles (white regions). These observations suggest that the inert ZrO_2 particles act as heterogeneous nucleation centers within the glass matrix, promoting diopside formation and accelerating the crystallization process. Interestingly, when ZrO_2 particles with diameters of 2 μm and 50 nm were introduced, the crystallization activation energy of the composite sealants first increased with rising ZrO_2 content, reaching a maximum at 30 wt%. This behavior can be attributed to the relatively uniform dispersion of ZrO_2 particles at lower concentrations, which impedes crystal growth and thereby increases the energy required for crystallization.[67,68] However, at loadings above 30 wt%, particularly with 50 nm ZrO_2, the high surface area and elevated surface energy of the nanoparticles induced agglomeration. This aggregation created localized energy-rich regions that facilitated nucleation, resulting in a sharp decrease in E_c. In contrast, the incorporation of 200 nm ZrO_2 particles led to a monotonic decrease in E_c with increasing particle content. BSE characterization indicates that ZrO_2 particles of this size remain more homogeneously dispersed, providing uniformly distributed heterogeneous nucleation sites. The continuous reduction in E_c can therefore be attributed to an optimal balance between surface reactivity and dispersion stability at this intermediate particle size. Such a balance ensures a sustained supply of effective nucleation centers and a progressive lowering of the crystallization energy barrier.

The crystalline phase composition of all composite sealing samples was quantified by semi-quantitative analysis of XRD patterns using JADE 9 software, and the corresponding volume fractions of diopside and ZrO_2 are summarized in Table 7. The results reveal a systematic evolution of phase composition with increasing ZrO_2 content. Specifically, as the ZrO_2 loading increases from 10 wt% to 40 wt%, the volume fraction of diopside gradually decreases from 26.9% to 15.4%, while that of ZrO_2 increases from 1.9% to 8.4%, regardless of particle size. This behavior demonstrates that the crystallization process is strongly affected by the introduction of inert ZrO_2 particles, which modify the nucleation environment and crystallization kinetics. From the perspective of crystallization kinetics, the addition of ZrO_2 significantly reduces E_c and generates a high density of heterogeneous nucleation sites within the glass matrix, establishing a nucleation-dominated crystallization regime. Consequently, a large number of fine diopside nuclei form rapidly during the early stage of heat treatment. However, the total supply of network-modifying cations (*e.g.*, Ca^{2+} and Mg^{2+}) available for crystal growth is intrinsically limited. As the nuclei density increases sharply, the material available to each nuclei becomes insufficient, thereby restricting subsequent crystal growth. This leads to a microstructure characterized by a high number density of diopside crystallites but substantially reduced grain size, which ultimately results in a lower overall diopside volume fraction despite the enhanced nucleation kinetics. In parallel, from a microstructural redistribution perspective, increasing ZrO_2 content progressively occupies a larger fraction of the composite volume. In particular, 200 nm ZrO_2 particles form a RPF that constrains the continuous glass phase and disrupts the development of an extended crystalline network, further limiting the space available for diopside nuclei growth. These mechanisms are directly corroborated by

Table 7 Volume fraction of the diopside and ZrO_2 phase in composite sealants after heat treatment at 850 °C for 4 hours determined by semi-quantitative analysis

Sample	Volume fraction of diopside (%)	Volume fraction of ZrO_2 (%)
GCZ10 $d = 2$ μm	26.9	1.9
GCZ10 $d = 200$ nm	26.6	2.1
GCZ10 $d = 50$ nm	26.9	1.9
GCZ20 $d = 2$ μm	23.0	4.1
GCZ20 $d = 200$ nm	22.6	4.4
GCZ20 $d = 50$ nm	22.9	4.2
GCZ30 $d = 2$ μm	19.2	6.3
GCZ30 $d = 200$ nm	18.9	6.4
GCZ30 $d = 50$ nm	19.4	6.2
GCZ40 $d = 2$ μm	15.9	8.2
GCZ40 $d = 200$ nm	15.4	8.4
GCZ40 $d = 50$ nm	15.7	8.3

Table 8 Coefficient of thermal expansion (α) of all samples

Sample	α ($\times 10^{-6}$ K^{-1}) 850 °C, 4 h	α ($\times 10^{-}$ K^{-1}) 850 °C, 20 h
GC	10.5	9.8
GCZ10 $d = 2$ μm	9.5	9.6
GCZ10 $d = 200$ nm	9.8	10.1
GCZ10 $d = 50$ nm	9.3	10.0
GCZ20 $d = 2$ μm	9.3	9.3
GCZ20 $d = 200$ nm	9.7	10.3
GCZ20 $d = 50$ nm	9.0	8.7
GCZ30 $d = 2$ μm	9.4	9.7
GCZ30 $d = 200$ nm	9.0	9.9
GCZ30 $d = 50$ nm	10.8	9.2
GCZ40 $d = 2$ μm	9.6	10.8
GCZ40 $d = 200$ nm	9.5	11.3
GCZ40 $d = 50$ nm	10.4	11.5

backscattered SEM observations (Fig. S44–S56), which show that the diopside grains in the ZrO_2-containing composites are markedly finer than those in the GC sample, in excellent agreement with the above crystallization-kinetics analysis.

It is observed that the CTE of all samples fall within the range of 9.0–11.5 $\times$ 10^{-6} K^{-1} (Table 8), meeting the fundamental requirements for SOFC sealants. In summary, the observed CTE trends are strongly governed by the combined effects of ZrO_2 incorporation and heat-treatment duration, reflecting the dynamic microstructural transformations occurring within the material.

After a 4-hour heat treatment at 850 °C, the CTE of the composite sealants decreases with the addition of ZrO_2, indicating that the presence of the ZrO_2 phase effectively suppresses the thermal deformation sensitivity of the composite sealant. As discussed in former part (E_c analysis), this phenomenon is directly linked to the heterogeneous nucleation effect of ZrO_2. The introduction of ZrO_2 significantly lowers the crystallization energy barrier, thereby promoting the rapid formation of numerous fine diopside nuclei during the initial stage of heat treatment. This accelerated nucleation process consumes substantial amounts of network-modifying cations (*e.g.*, Ca^{2+} and Mg^{2+}) from the glass matrix, resulting in a more rigid residual glass network. The enhanced structural rigidity restricts atomic vibration amplitudes during heating, consequently reducing the material's thermal expansion capability and leading to a pronounced decrease in CTE after short-term heat treatment.[69] Furthermore, inert ZrO_2 particles embedded within the glass network along with the precipitated diopside phase, create a highly constrained composite network at the microscale. This multi-phase rigid network further limits thermal deformation and reinforces the suppression of thermal expansion. Notably, GCZ30, $d = 200$ nm sample exhibited lower CTE values than the glass-ceramic matrix, which aligns with the earlier analysis regarding the formation of RPF structure. This confirms the particular effectiveness of this particle size in constraining the material's thermal deformation.

Upon extending the dwell time at 850 °C to 20 h, the CTE evolution diverged. The CTE of the GC sample decreases from 10.5 to 9.8 $\times$ 10^{-6} K^{-1}. This reduction is attributed to the continuous precipitation of diopside phase from the glass phase in GC at 850 °C. In contrast, the CTE of the composite sealants exhibits a general increase after prolonged heat treatment. This behavior is associated with grain growth and coarsening processes accompanied by grain boundary migration, which induce further microstructural rearrangement among the ZrO_2, glass, and crystalline phases. Consequently, the initially highly constrained composite network gradually evolves into a more thermodynamically stable multiphase structure, leading to partial relaxation of the rigid constraints and a pronounced rebound in thermal expansion upon extended heat treatment.

4. Conclusions

In summary, the effects of ZrO_2 particle size and content on the sintering and crystallization behaviors of base glass (GC) sealants were systematically investigated. Sintering analysis reveals that increasing ZrO_2 content effectively extends the sintering stage, initiating densification earlier and more gradually with 200 nm ZrO_2 showing the strongest influence in the temperature range of T_{FS} to T_{MS}. Viscosity analysis further demonstrates that 2 μm and 200 nm ZrO_2 particles increase the resistance to viscous flow, whereas 50 nm ZrO_2 particles form agglomerates at high loading, reducing viscosity. SEM imaging indicates that 200 nm ZrO_2 forms a three-dimensional rigid percolation framework (RPF), segmenting the amorphous glass, enhancing interfacial interactions, and facilitating pore healing, while other particle sizes are less effective due to aggregation. XRD combined with crystallization kinetics analysis confirm that ZrO_2 does not alter the phase composition but acts as heterogeneous nucleation sites, promoting diopside formation. For 2 μm and 50 nm particles, E_c initially increases at low content and decreases at higher loadings due to agglomeration, whereas 200 nm particles consistently lower E_c, reflecting optimal dispersion and sustained nucleation efficiency. Semi-quantitative analysis of the crystalline volume fractions demonstrates that the introduction of ZrO_2 markedly promotes the formation of numerous crystalline nuclei within the glass matrix. Although the crystallization barrier E_c is significantly reduced, the excessive nuclei struggle to fully grow due to constrained space and finite availability of network-modifying species, resulting in substantially finer crystalline grains compared with the GC sample. Finally, thermal expansion measurements confirm that the ZrO_2-modified silicate glass composite sealants exhibit coefficients of thermal expansion fully compatible with the requirements for SOFC sealing applications. Overall, ZrO_2 particle characteristics critically modulate densification, viscosity, and crystallization, providing a pathway to optimize glass–ceramic sealants for high-performance, thermally stable SOFC operation.

Author contributions

Shuai Yuan: conceptualization, data curation, formal analysis, funding acquisition, investigation, methodology, validation, visualization, writing original draft preparation, and writing review & editing. Haozhen Li: funding acquisition, investigation, resources and supervision. Hao Shi: resources and supervision. Yuxuan Fei: data curation and software. Hengyong Tu: supervision and writing review & editing. Chao Ma: supervision, resources and writing review & editing. Lei Zhu: project administration, resources and writing review & editing. Zhen Huang: resources and writing review & editing.

Conflicts of interest

There are no conflicts to declare.

Data availability

All data supporting the findings of this study are available within the paper and supplementary information (SI). supplementary information: sintering curves and relative first derivative curves of different samples; characteristic temperature and shrinkage rate of different samples; DSC curves of different

samples; porosity calculation results of different samples; SEM & EDS images of different samples; calculation patterns of E_η, F, E_c, $\langle n \rangle$ of different samples and dilatometric thermograph of different samples in a PDF format. Supplementary information is available. See DOI: https://doi.org/10.1039/d5ra08813e.

Acknowledgements

This work was financially supported by the National Natural Science Foundation of China (nos. 52394204 and 52394205), Shanghai Municipal Science and Technology Major Project, Shanghai Pilot Program for Basic Research—Shanghai Jiao Tong University (no. 21TQ1400207), Shanghai Science and Technology Innovation Program (no. 21DZ1206400), and Startup Fund for Young Faculty at SJTU (22X010503814).

References

1 T. Sira and M. Ostenstad, Temperature and flow distributions in planar SOFC stacks, *ECS PVs*, 1993, **1993**, 851.
2 X. V. Nguyen, C. T. Chang, G. B. Jung, S. H. Chan, W. T. Lee, S. W. Chang and I. C. Kao, Study of sealants for SOFC, *Int. J. Hydrogen Energy*, 2016, **41**, 21812–21819.
3 K. S. Weil, C. A. Coyle, J. S. Hardy, J. Y. Kim and G. Xia, Alternative planar SOFC sealing concepts, *Fuel Cell. Bull.*, 2004, **2004**, 11–16.
4 Y. Zhao, J. Malzbender and S. M. Gross, The effect of room temperature and high temperature exposure on the elastic modulus, hardness and fracture toughness of glass ceramic sealants for solid oxide fuel cells, *J. Eur. Ceram. Soc.*, 2011, **31**, 541–548.
5 S. Kim, I. Jang, C. Kim, H. Lee, T. Song, H. Yoon and U. Paik, Enhanced reliability of planar-type solid oxide fuel cell stack incorporating leakage gas induction channels, *Int. J. Hydrogen Energy*, 2020, **45**, 11834–11841.
6 Y. S. Chou and J. W. Stevenson, Mid-term stability of novel mica-based compressive seals for solid oxide fuel cells, *J. Power Sources*, 2003, **115**, 274–278.
7 J. W. Fergus, Sealants for solid oxide fuel cells, *J. Power Sources*, 2005, **147**, 46–57.
8 J. Thijssen, M. C. Williams and H. Quedenfeld, *Fuel Cell Handbook, EG&G Technical Services Inc., US Department of Energy, Office of Fossil Energy, National Energy Technology Laboratory*, Morgantown, West Virginia (USA), 7th edn, 2004.
9 C. Lara, M. J. Pascual and A. Durán, Glass and glass-ceramic sealants for Solid Oxide Fuel Cells (SOFC), *Bol. Soc. Esp. Ceram. Vidrio*, 2003, **42**, 133–143.
10 K. S. Weil, The state-of-the-art in sealing technology for solid oxide fuel cells, *JOM*, 2006, **58**, 37–44.
11 M. K. Mahapatra and K. Lu, Glass-based seals for solid oxide fuel and electrolyzer cells–a review, *Mater. Sci. Eng., R*, 2010, **67**, 65–85.
12 J. Yan, T. Zhang, H. Tao, H. Zhan and Y. Yue, Structure, crystallization, and performances of alkaline-earth boroaluminosilicate sealing glasses for SOFCs, *J. Am. Ceram. Soc.*, 2021, **104**, 2560–2570.
13 H. Ren, W. Ge, L. Chen, H. Peng, F. Meng, H. Lin and Y. Jin, Low thermal stress and excellent gas tightness in BaO–CaO–Al_2O_3–B_2O_3–SiO_2 glass-ceramic for long-term ITSOFC application, *J. Am. Ceram. Soc.*, 2025, **108**, e20197.
14 M. S. Salinigopal, N. Gopakumar, P. S. Anjana and O. P. Pandey, Rare earth added barium alumino borosilicate glass-ceramics as sealants in solid oxide fuel cells, *J. Non-Cryst. Solids*, 2022, **576**, 121242.
15 H. Javed, E. Zanchi, F. D'Isanto, C. Bert, D. Ferrero, M. Santarelli and F. Smeacetto, Novel SrO-Containing Glass-Ceramic Sealants for Solid Oxide Electrolysis Cells (SOEC): Their Design and Characterization under Relevant Conditions, *Materials*, 2022, **15**, 5805.
16 M. J. Snyder, M. G. Mesko and J. E. Shelby, Volatilization of boron from E-glass melts, *J. Non-Cryst. Solids*, 2006, **352**, 669–673.
17 Y. N. Pitak and Y. V. Churilova, Subsolidus Structure of the System Al_2O_3–SiO_2–MgO–P_2O_5 (A Review), *Glass Ceram.*, 2003, **60**, 150–153.
18 M. Brochu, B. D. Gauntt, R. Shah, G. Miyake and R. E. Loehman, Comparison between barium and strontium-glass composites for sealing SOFCs, *J. Eur. Ceram. Soc.*, 2006, **26**, 3307–3313.
19 F. Heydari, A. Maghsoudipour, Z. Hamnabard and S. Farhangdoust, Mechanical properties and microstructure characterization of zirconia nanoparticles glass composites for SOFC sealant, *Mater. Sci. Eng., A*, 2012, **552**, 119–124.
20 S. M. Gross, T. Koppitz, J. Remmel, J. B. Bouche and U. Reisgen, Joining properties of a composite glass-ceramic sealant, *Fuel Cell. Bull.*, 2006, **2006**, 12–15.
21 K. A. Nielsen, M. Solvang, S. B. L. Nielsen, A. R. Dinesen, D. Beeaff and P. H. Larsen, Glass composite seals for SOFC application, *J. Eur. Ceram. Soc.*, 2007, **27**, 1817–1822.
22 P. Rao and R. N. Singh, Sintering and thermal expansion behaviors of glass and glass–YSZ composites as self-repairable seals for SOFC, *J. Am. Ceram. Soc.*, 2023, **106**, 157–165.
23 R. Li, J. Yang, D. Yan, J. Pu, B. Chi and J. Li, Performance of Al_2O_3 particle reinforced glass-based seals in planar solid oxide fuel cells, *Ceram. Int.*, 2021, **47**, 7504–7510.
24 M. O. Prado, E. D. Zanotto and R. Müller, Model for sintering polydispersed glass particles, *J. Non-Cryst. Solids*, 2001, **279**, 169–178.
25 J. Frenkel, Viscous flow of crystalline bodies under the action of surface tension, *J. Phys.(USS R)*, 1945, **9**, 385.
26 B. Li, Q. Long and D. Duan, Effects of ZrO_2 on properties of BaO–Al_2O_3–B_2O_3–SiO_2 composites for LTCC applications, *J. Mater. Sci.:Mater. Electron.*, 2016, **27**, 2824–2829.
27 M. Ghaffari, P. Alizadeh and M. Rahimipour, Sintering behavior and mechanical properties of mica-diopside glass–ceramic composites reinforced by nano and micro-sized zirconia particles, *J. Non-Cryst. Solids*, 2012, **358**, 3304–3311.
28 C. Blaeß and R. Müller, Viscous crack healing in soda–lime–magnesium–silicate–ZrO_2 glass matrix composites, *J. Am. Ceram. Soc.*, 2024, **107**, 7212–7223.

29 S. Gali, A. Arjun and H. Premkumar, Zirconia toughened fluorosilicate glass-ceramics for dental prosthetic restorations, *Mater. Chem. Phys.*, 2024, **324**, 129703.
30 A. Shearer, M. Montazerian, B. Deng, J. J. Sly and J. C. Mauro, Zirconia-containing glass-ceramics: From nucleating agent to primary crystalline phase, *Int. J. Ceram. Eng. Sci.*, 2024, **6**, e10200.
31 X. Wang, R. Li, D. Gu, L. Tian, D. Yan, J. Pu, T. Geng, B. Chi and J. Li, Crystallization kinetics and phase transformation of glass-ceramic seals for solid oxide fuel cell application, *J. Alloys Compd.*, 2019, **786**, 544–550.
32 F. Smeacetto, A. De Miranda, A. Chrysanthou, E. Bernardo, M. Secco, M. Bindi, M. Salvo, A. G. Sabato and M. Ferraris, Novel glass-ceramic composition as sealant for SOFCs, *J. Am. Ceram. Soc.*, 2014, **97**, 3835–3842.
33 B. Cela, S. Sillapawatana, S. M. Gross, T. Koppitz and R. Conradt, Influence of filler additives on the effective viscosity of glass-ceramic composite sealants, *J. Univ. Chem. Technol. Metall.*, 2012, **47**, 449–458.
34 H. Scholze, Influence of viscosity and surface tension on hot-stage microscopy measurements on glasses, *Ber. Dtsch. Keram. Ges.*, 1962, **391**, 63–68.
35 C. Lara, M. J. Pascual, M. O. Prado and A. Durán, Sintering of glasses in the system RO–Al_2O_3–BaO–SiO_2 (R= Ca, Mg, Zn) studied by hot-stage microscopy, *Solid State Ionics*, 2004, **170**, 201–208.
36 M. Lasocka, The effect of scanning rate on glass transition temperature of splat-cooled $Te_{85}Ge_{15}$, *Mater. Sci. Eng.*, 1976, **23**, 173–177.
37 L. Liu, L. Luo, L. Wang, L. Cheng, X. Xu, Y. Yu, Y. Qin and Y. Wu, Exploring the functions of Al_2O_3 in the transition of $BaAl_2SiO_8$ precipitated from CaO-BaO-Al_2O_3-B_2O_3-SiO_2 sealing glass for IT-SOFCs, *Mater. Ceram.*, 2019, **71**, 368–377.
38 R. Wang, Z. Lü, C. Liu, R. Zhu, X. Huang, B. Wei, N. Ai and W. Su, Characteristics of a SiO_2–B_2O_3–Al_2O_3–$BaCO_3$–PbO_2–ZnO glass–ceramic sealant for SOFCs, *J. Alloys Compd.*, 2007, **432**, 189–193.
39 R. G. Beaman, Relation between (apparent) second-order transition temperature and melting point, *J. Polym. Sci.*, 1952, **9**, 470–472.
40 W. Vogel, in *Glass Chemistry*, ed. W. Vogel, Springer, Berlin, Heidelberg, 2nd edn, 1994, pp. 22–33.
41 G. S. Fulcher, Analysis of recent measurements of the viscosity of glasses, *J. Am. Ceram. Soc.*, 1925, **8**, 339–355.
42 M. J. Pascual, A. Duran and M. O. Prado, A new method for determining fixed viscosity points of glasses, *Phys. Chem. Glasses*, 2005, **46**, 512–520.
43 A. S. Alzahrani, Syntheses and characterization of twofold nepheline-combeite glass-ceramics for dental application, *J. Non-Cryst. Solids*, 2022, **596**, 121877.
44 C. Blaeß and R. Müller, Fast crack healing in glass-matrix composites with rigid filler percolation frameworks, *J. Am. Ceram. Soc.*, 2025, **108**, e20386.
45 S. Mahadevan, A. Giridhar and A. K. Singh, Calorimetric measurements on As-Sb-Se glasses, *J. Non-Cryst. Solids*, 1986, **88**, 11–34.
46 H. E. Kissinger, Reaction kinetics in differential thermal analysis, *Anal. Chem.*, 1957, **29**, 1702–1706.
47 H. E. Kissinger, Variation of peak temperature with heating rate in differential thermal analysis, *J. Res. Natl. Bur. Stand*, 1956, **57**, 217–221.
48 M. M. Wakkad, E. K. Shokr and S. H. Mohamed, Optical and calorimetric studies of Ge–Sb–Se glasses, *J. Non-Cryst. Solids*, 2000, **265**, 157–166.
49 G. Kaur, O. P. Pandey and K. Singh, Glass stability and effect of heat-treatment duration on chemical interaction between calcium lanthanum borosilicate glass sealant and electrolytes, *J. Electrochem. Soc.*, 2012, **159**, F717.
50 G. Kaur, O. P. Pandey and K. Singh, Microstructural analysis of interfaces between lanthanum contained glass and two different electrolytes for SOFC applications, *Fuel Cells (Weinheim, Ger.)*, 2012, **12**, 739–748.
51 C. Blaeß and R. Müller, Viscous healing of Vickers indentation–induced cracks in glass, *J. Am. Ceram. Soc.*, 2023, **106**, 5795–5805.
52 T. A. Vilgis, Strong and fragile glasses: A powerful classification and its consequences, *Phys. Rev. B*, 1993, **47**, 2882.
53 R. Böhmer and C. A. Angell, in *Disorder Effects on Relaxational Processes: Glasses, Polymers, Proteins*, ed. R. Richert and A. Bluemen, Springer, Berlin, Heidelberg, 1st edn, 1994, pp. 11–54.
54 T. D. Mel'Nichenko, V. M. Rizak, T. N. Mel'Nichenko and V. I. Fedelesh, Parameters of the fluctuation free volume theory for glasses in the Ge-As-Se system, *Glass Phys. Chem.*, 2004, **30**, 406–414.
55 R. Li, Y. Lu, Y. Yu, C. Guan, G. Xiao, J. Pu and J. Wang, Thermal performance of glass-based seals for reversible solid oxide cell: Effect of Al_2O_3 ceramic addition on the crystallization behavior, *Ceram. Int.*, 2024, **50**, 6481–6489.
56 J. A. Augis and J. E. Bennett, Calculation of the Avrami parameters for heterogeneous solid state reactions using a modification of the Kissinger method, *J. Therm. Anal.*, 1978, **13**, 283–292.
57 J. Jin, F. Li, G. Yin, X. Wang and P. Gong, Influence of substitution of Cu by Ni on the crystallization kinetics of TiZrHfBeCu high entropy bulk metallic glass, *Thermochim. Acta*, 2020, **690**, 178650.
58 Y. Bai, L. Peng, Q. Zhu and Z. Hao, Non-isothermal crystallization kinetics of stoichiometric lithium disilicate-based glasses with Al_2O_3 additives, *J. Non-Cryst. Solids*, 2016, **445**, 116–122.
59 K. Tanaka, Y. Okada, M. Sugi, S. Iizima and M. Kikuchi, Kinetics of growth of conductive filament in As-Te-Ge glasses, *J. Non-Cryst. Solids*, 1973, **12**, 100–114.
60 L. Liu, L. Luo, L. Wang, L. Cheng, X. Xu, Y. Yu, Y. Qin and Y. Wu, Study on non-isothermal crystallization kinetics of the BaO-CaO-Al_2O_3-B_2O_3-SiO_2 glass for IT-SOFCs sealing, *Ceram. Int.*, 2018, **44**, 21277–21283.
61 M. Erol, S. Küçükbayrak and A. Ersoy-Mericboyu, Influence of particle size on the crystallization kinetics of glasses produced from waste materials, *J. Non-Cryst. Solids*, 2011, **357**, 211–219.

62 A. Karamanov, I. Avramov, L. Arrizza, R. Pascova and I. Gutzow, Variation of Avrami parameter during non-isothermal surface crystallization of glass powders with different sizes, *J. Non-Cryst. Solids*, 2012, **358**, 1486–1490.
63 S. Rodríguez-López and M. J. Pascual, Sintering/crystallization and viscosity of sealing glass-ceramics, *Crystals*, 2021, **11**, 737.
64 I. W. Donald, Crystallization kinetics of a lithium zinc silicate glass studied by DTA and DSC, *J. Non-Cryst. Solids*, 2004, **345**, 120–126.
65 T. Ozawa, Kinetics of non-isothermal crystallization, *Polymer*, 1971, **12**, 150–158.
66 W. Zhang, F. He, J. Xie, X. Liu, D. Fang, H. Yang and Z. Luo, Crystallization mechanism and properties of glass ceramics from modified molten blast furnace slag, *J. Non-Cryst. Solids*, 2018, **502**, 164–171.
67 M. Guo, X. Zhang, Y. Li, M. Andersson, Z. Yang and S. Peng, High gas tightness ZrO_2-added silicate glass sealant with low thermal stress for solid oxide fuel cells, *Ceram. Int.*, 2023, **49**, 19708–19716.
68 X. Wang, R. Li, T. Hu, M. Wang, L. Zhang and C. Zhao, Mechanical behavior of YSZ-glass composite seals for solid oxide fuel cell application, *Ceram. Int.*, 2023, **49**, 995–1001.
69 J. E. Shelby, *Introduction to Glass Science and Technology*, The Royal Society of Chemistry, Cambridge , UK, 2nd edn, 2020.